



# OPEN Direct evidence of terahertz emission arising from anomalous Hall effect

Venkatesh Mottamchetty<sup>1</sup>, Parul Rani<sup>2</sup>, Rimantas Brucas<sup>1</sup>, Anders Rydberg<sup>1,2</sup>, Peter Svedlindh<sup>1</sup>✉ & Rahul Gupta<sup>1,2</sup>✉

A detailed understanding of the different mechanisms being responsible for terahertz (THz) emission in ferromagnetic (FM) materials will aid in designing efficient THz emitters. In this report, we present direct evidence of THz emission from single layer  $\text{Co}_{0.4}\text{Fe}_{0.4}\text{B}_{0.2}$  (CoFeB) FM thin films. The dominant mechanism being responsible for the THz emission is the anomalous Hall effect (AHE), which is an effect of a net backflow current in the FM layer created by the spin polarized current reflected at the interfaces of the FM layer. The THz emission from the AHE-based CoFeB emitter is optimized by varying its thickness, orientation, and pump fluence of the laser beam. Results from electrical transport measurements show that skew scattering of charge carriers is responsible for the THz emission in the CoFeB AHE-based THz emitter.

The region of the electromagnetic spectrum that lies between near microwave and far-infrared radiation is the so-called Terahertz (THz) radiation or THz gap, i.e. typically frequencies between 100 GHz and 30 THz. Terahertz radiation finds applications in various fields, such as medicine, security, etc.<sup>1,2</sup>. Photoconductive switching, optical rectification, transient photo-current in air plasma, and difference frequency generation constitute techniques that are employed for the generation of THz radiation<sup>3–13</sup>. Moreover, THz emission from magnetic materials, utilizing the spin degree of freedom, has recently gained popularity as a promising framework for the generation of broadband radiation without any phonon absorption gaps and with intensity comparable to the standard zinc telluride THz source<sup>14,15</sup>.

There are several possible mechanisms that can explain THz generation in spin-based systems. Beaupaire et al.<sup>16</sup> discovered ultrafast demagnetization (UDM) in 1996, showing that a ferromagnetic (FM) Ni film when demagnetized on a subpicosecond time scale by a femtosecond (fs) laser pulse excitation generates THz radiation<sup>17</sup>. The THz radiation is in this case proportional to the second time-derivative of the magnetization<sup>18</sup> and shows a linear dependence on the thickness of the FM layer. Recently, Kampfrath et al.<sup>14,19</sup> discovered an alternative mechanism for THz generation, which utilizes the inverse spin Hall effect (iSHE) or inverse Rashba Edelstein effect (iREE). Here, the generation mechanism requires a magnetic heterostructure consisting of an FM layer and a non-magnet (NM) layer that possesses a high spin-to-charge (S2C) conversion efficiency. In this mechanism, the amplitude of the THz emission is highly dependent on the S2C conversion efficiency. Recently, it has been shown that THz emitters can be designed using a single FM layer, which utilizes the anomalous Hall effect (AHE) phenomenon<sup>20–23</sup>. On the one hand, the UDM mechanism relies on bulk properties of a single FM layer, while on the other hand the AHE mechanism corresponds to a combined effect of interface and bulk properties, which will be further discussed below.

A fs laser pulse when incident on a FM layer will excite hot electrons in the FM layer. The system achieves equilibrium through electron–electron, electron–phonon and electron–magnon interactions. Before attaining the equilibrium with respect to electron–electron interactions, the hot electrons acquire a velocity of order  $10^6$  m/s and move within the FM layer in a super-diffusive manner<sup>24,25</sup>. When reaching the FM/dielectric interfaces as indicated in Fig. 1, electrons reflect back from the interfaces to form a net backflow current ( $j_{bf}$ ) along the film thickness direction<sup>25</sup>. In the presence of the AHE,  $j_{bf}$  is converted to a transient current ( $j_t$ ) defined as  $j_t = \theta_{AHE}(m \times j_{bf})$ , where  $\theta_{AHE}$  and  $m$  are the anomalous Hall angle and the magnetization direction, respectively. The net backflow current depends on the dielectric properties of the interfaces, their roughness and properties of the FM layer, such as  $\theta_{AHE}$  and  $m$ .

<sup>1</sup>Department of Materials Science and Engineering, Uppsala University, Box 35, 751 03 Uppsala, Sweden. <sup>2</sup>Department of Physics and Astronomy, Uppsala University, Box 516, 75120 Uppsala, Sweden. ✉email: peter.svedlindh@angstrom.uu.se; rahul.gupta@angstrom.uu.se



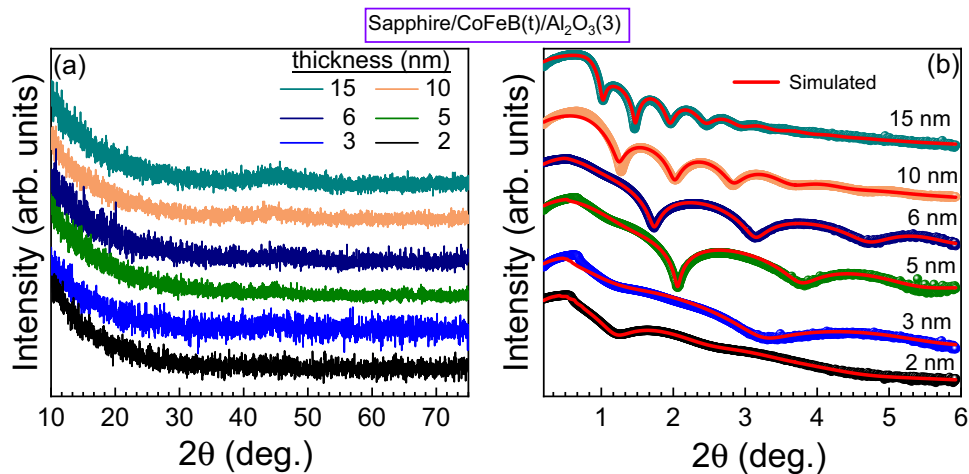


**Figure 2.** (a) XRD spectra for our emitters with different nominal thicknesses of CoFeB, and (b) XRR spectra for our emitters with different nominal thicknesses of CoFeB. Colored symbols and red lines correspond to experimental observed and simulated data, respectively.

from a substrate/CoFeB (5 nm)/cap emitter with different magnetization polarities and different pumping sides. Note that the polarity of the THz waveform is reversed when reversing the magnetization direction while keeping the pumping side the same (i.e., the net backflow current direction is the same). Thus, the THz emission is clearly of magnetic origin. Moreover, the THz waveform polarity is reversed when the sample is flipped, which is attributed to the AHE due to a change in direction of the net backflow current. It should be noted that the waveform polarities will be the same for the UDM mechanism due to similar magnetization dynamics. To distinguish between the contributions from the AHE and UDM to the THz emission, the approach of Liu et al.<sup>22</sup> was followed by comparing the THz waveform emitted from the capping and substrate sides of the emitter. The difference between these waveforms reveals that the AHE is the dominant effect, contributing ~ 93% of the THz emission, while UDM contributes only ~ 7%. Thus, this clearly indicates that the dominant THz emission mechanism for the CoFeB emitters is the AHE, which is a combination of bulk and interface effects. The dependence of the THz peak-to-peak amplitude ( $E_{THz}^{P-P}$ ) on the laser pump fluence is shown in the inset of Fig. 3b. Note that  $E_{THz}^{P-P}$  shows a linear behaviour up to 0.18 mJ/cm<sup>2</sup> pump fluence, thus the pump fluence was fixed at 0.18 mJ/cm<sup>2</sup> for the thickness-dependent study as discussed below.

The CoFeB thickness dependence of the AHE was measured to further investigate the relationship between the THz emission and the AHE. A schematic of the AHE measurement using a Hall bar geometry is depicted in the inset of Fig. 4b. A longitudinal DC current (4 mA) was applied and the transverse voltage (i.e., Hall voltage) was measured while sweeping the out-of-plane magnetic field. In Fig. 4a, the Hall resistivity ( $\rho_{xy}$ ) contains contributions from the AHE and the ordinary Hall effect. The anomalous Hall resistivity ( $\rho_{xy}^{AH}$ ), defined as the saturation value of  $\rho_{xy}$ , was extracted after subtracting the contribution from the ordinary Hall effect; the thickness dependence of  $\rho_{xy}^{AH}$  is shown in Fig. 4b. The CoFeB thickness dependence of the longitudinal resistivity ( $\rho_{xx}$ ) was also measured, which follows an exponential behavior as shown in Fig. 4c. The ratio of the anomalous Hall resistivity to the longitudinal resistivity defines the anomalous Hall angle ( $\theta_{AHE} = \rho_{xy}^{AH} / \rho_{xx}$ ). A comparison of the  $\theta_{AHE}$  and the THz peak-to-peak amplitude as a function of CoFeB thickness is shown in Fig. 4d. Both  $\theta_{AHE}$  and  $E_{THz}$  increase and follow a similar trend up to about 5 nm CoFeB thickness. However, while  $\theta_{AHE}$  saturates with a further increase of CoFeB thickness,  $E_{THz}^{P-P}$  decreases. The increase of the THz emission amplitude up to 5 nm CoFeB thickness may also be explained by that the applied field (~ 85 mT) during the THz emission

$t_{CoFeB}^N$	$\sigma_{substrate/CoFeB}$ ( $\pm 0.05$ )	$t_{CoFeB}^E$ ( $\pm 0.05$ )	$\sigma_{CoFeB/capping}$ ( $\pm 0.05$ )	$t_{Al_2O_3}^E$ ( $\pm 0.05$ )	$\sigma_{capping/air}$ ( $\pm 0.05$ )
2	0.27	1.89	0.91	3.49	1.21
3	0.55	3.26	0.82	3.46	1.89
5	0.69	5.16	0.77	3.19	1.99
6	0.59	6.13	0.80	3.20	1.99
10	0.28	11.33	0.87	3.09	1.19
15	0.20	15.95	1.35	3.95	1.84

**Table 1.** Comparison of nominal ( $t_{CoFeB}^N$ ) and GenX<sup>26</sup> extracted thickness ( $t_{CoFeB}^E$ ) from XRR analysis. The thickness and roughness are in nm.

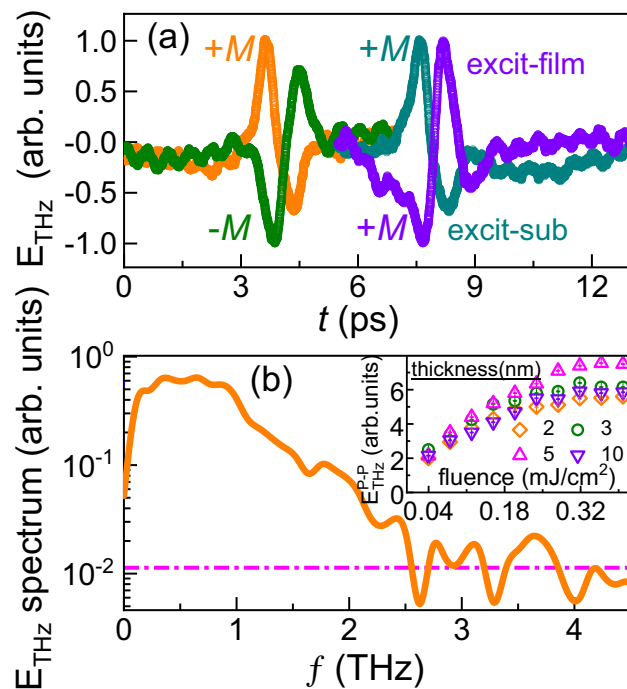


**Figure 3.** (a) Peaks at  $\sim 4$  ps: THz waveform in time-domain ( $t$ ) for substrate/CoFeB (5 nm)/cap emitter with different magnetization directions ( $\pm M$ ) when pumping from substrate side. Peaks at  $\sim 8$  ps: THz waveform pumping from the capping layer and substrate sides while keeping the same magnetization direction. Time scale is shifted for better visualization of both cases. (b) Fast Fourier transform of THz electric field and the inset shows THz peak-to-peak amplitude for substrate/CoFeB( $t_{\text{CoFeB}}$  nm)/cap emitters as a function of pump fluence.

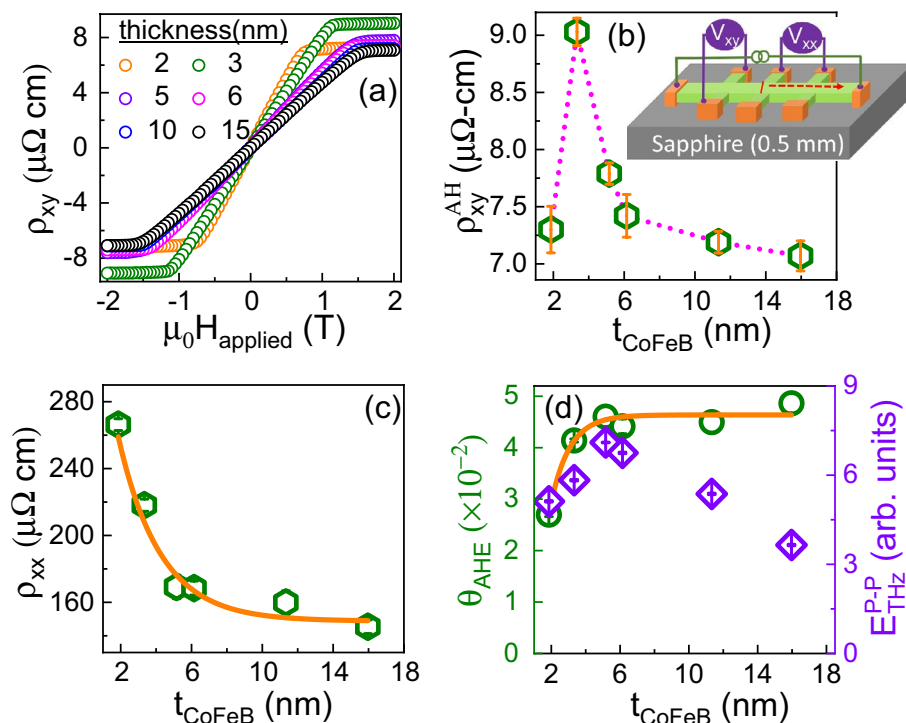


**Figure 4.** Results from Hall ( $\rho_{xy}$ ) and longitudinal ( $\rho_{xx}$ ) resistivity measurements on CoFeB films with different thickness. (a)  $\rho_{xy}$  vs. applied magnetic field ( $\mu_0 H_{\text{applied}}$ ), (b)  $\rho_{xy}^{\text{AH}}$  vs.  $t_{\text{CoFeB}}$  where  $\rho_{xy}^{\text{AH}}$  corresponds to the saturation value of  $\rho_{xy}$ , (c)  $\rho_{xx}$  vs.  $t_{\text{CoFeB}}$ , and (d) THz peak-to-peak amplitude (right y-axis) and anomalous Hall angle (left y-axis) vs.  $t_{\text{CoFeB}}$ .

experiment is not sufficient to completely saturate the CoFeB films as CoFeB may possess an out-of-plane or easy cone anisotropy in the low thickness regime. Therefore, in-plane magnetization hysteresis loops were measured for all films, clearly showing that this is not a valid explanation for the studied films; the magnetization for all CoFeB films saturates at magnetic fields smaller than 85 mT as shown in the inset of Fig. 5b. The decrease of the THz emission amplitude at larger CoFeB thickness can be explained by the fact that the spin current generated by the laser pulse scales as  $A/t_{\text{CoFeB}}$ <sup>15</sup>, where  $A$  is the absorption of the incident pump pulse by the emitter and  $t_{\text{CoFeB}}$  is the thickness of the CoFeB layer. Therefore, the absorption of the incident laser pulse was calculated by measuring the incident ( $P_{\text{inc}}$ ), reflected ( $P_{\text{ref}}$ ) and transmitted ( $P_{\text{trans}}$ ) powers in the optical range for all CoFeB films. The absorption was calculated from  $A = 1 - T - R$ , where  $T = P_{\text{trans}}/P_{\text{inc}}$  and  $R = P_{\text{ref}}/P_{\text{inc}}$  are the transmittance and reflectance, respectively. The absorption as a function of CoFeB thickness is shown in Fig. 5a, which decreases from 60 to 45% as the CoFeB thickness increases. Note that the change in absorption ( $\sim 33\%$ ) is not enough to explain the decrease of the THz emission ( $\sim 2$  times). Instead the results show that the decrease of the THz emission amplitude is dominated by the thickness effect (i.e., the Fabry–Perot cavity effect<sup>14,15</sup>). Furthermore, the self-absorption of THz radiation also leads to a decrease of the THz emission intensity in the large thickness regime. In our previous work<sup>15</sup>, we reported that the self-absorption scales as  $e^{-t_{\text{CoFeB}}/\zeta_{\text{THz}}}$ , where  $\zeta_{\text{THz}}$  is the effective inverse attenuation coefficient of the THz radiation. For metallic THz emitters,  $\zeta_{\text{THz}}$  ranges from 14 to 22 nm<sup>15,21,27</sup>. Therefore, the decrease of the THz emission intensity at larger thickness is a combined effect of thickness and self-absorption of THz radiation in the CoFeB-based emitter.

The experimental results confirm that the dominant mechanism for THz emission in CoFeB is the AHE. However, the AHE can have both intrinsic and extrinsic contributions. The intrinsic contribution for the AHE arises from the electronic band structure and the Berry phase<sup>28</sup>, which generally requires growth of epitaxial layers. A dominant intrinsic contribution to the AHE in our case is unlikely since the CoFeB films are amorphous in nature. Moreover, the extrinsic contribution originates from impurity scatterings such as side jump and skew scattering<sup>28</sup>. The anomalous Hall resistivity is expected to be proportional to the saturation magnetization ( $M_s$ )<sup>28</sup>, i.e.,  $\rho_{xy}^{\text{AH}} = R_s M_s$ , where  $R_s$  is the anomalous Hall coefficient.  $R_s$  increases linearly with  $\rho_{xx}$  for skew scattering (i.e.,  $R_s \propto \rho_{xx}$ ), while the dependence is parabolic for side jump scattering (i.e.,  $R_s \propto \rho_{xx}^2$ ). Therefore, the CoFeB thickness dependence of  $M_s$  was measured to be able to identify the dominant scattering mechanism for CoFeB; the results are shown in Fig. 5b. Figure 5c shows  $\rho_{xy}^{\text{AH}}/M_s$  versus  $\rho_{xx}$ , indicating a linear relationship. Here, the anomalous Hall resistance ( $R_s = \rho_{xy}^{\text{AH}}/M_s$ ) is significantly affected for 2 nm nominal CoFeB thickness, deviating strongly from the linear relationship observed at larger thickness. The deviation is enhanced by the magnetic dead layer (DL), which was calculated to be 0.59 nm (cf. Fig. 5d), resulting in an increased impact of interface

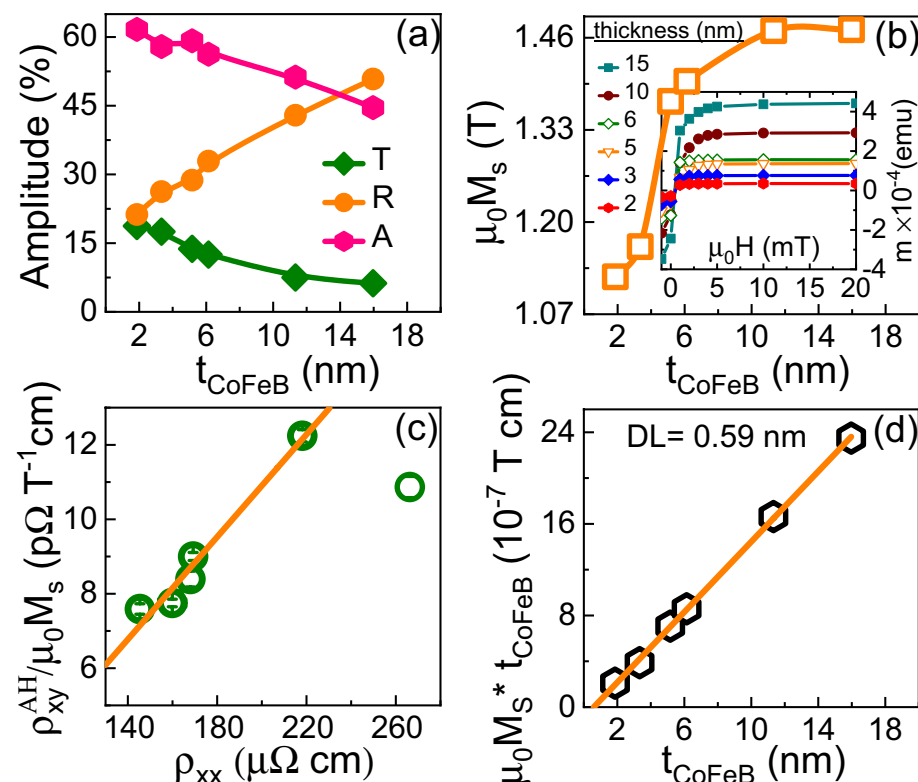


**Figure 5.** (a) Transmission ( $T$ ), reflectance ( $R$ ) and absorption ( $A$ ) vs.  $t_{\text{CoFeB}}$ . Solid lines are shown as guide to the eye. (b) Saturation magnetization  $\mu_0 M_s$  vs.  $t_{\text{CoFeB}}$ . Solid line is shown as guide to the eye. (c)  $\rho_{xy}^{\text{AH}}/\mu_0 M_s$  vs.  $\rho_{xx}$ . Solid line is a linear fit excluding the result for the 2 nm thick film. (d)  $\mu_0 M_s \cdot t_{\text{CoFeB}}$  vs.  $t_{\text{CoFeB}}$ . Solid line is a linear fit to the experimental data.



scattering on the charge carrier transport in the low thickness regime. Additionally, the substrate/CoFeB interface roughness is found to be smaller than that of the CoFeB/capping interface (cf. Table 1). This indicates that the CoFeB/capping interface plays a dominant role for the longitudinal resistivity at low film thickness. The deviation for the 2 nm thick CoFeB emitter is thus explained by that the electrical transport at such low thickness is dominated by surface/interface scattering and that this scattering may not be an efficient mechanism for AHE since it is mostly spin-independent<sup>20</sup>. Note that the anomalous Hall angle measurement is based on the diffusive transport model, while the THz emission involved the super-diffusive transport model. The conduction electrons involved in the super-diffusive transport model are located close to the Fermi level, making them equivalent to the conduction electrons in the diffusive transport model. Seifert et al.<sup>29</sup> demonstrated that the anomalous Hall conductivity and anomalous Hall angle are frequency-independent up to 40 THz, and therefore consistent with the DC anomalous Hall conductivity within an error bar of 2%.

## Conclusions

To summarize, we provide direct evidence that THz emission in CoFeB thin films is a consequence of the anomalous Hall effect. The THz emission from single layer CoFeB films has been studied as a function of CoFeB thickness and the laser pump fluence. It is shown that the THz emission is a result of the nonthermal spin-polarized currents created by the laser pulse, which are reflected at the interfaces of the ferromagnetic layer, forming a net backflow current that is converted to a transverse charge current via the anomalous Hall effect. Results from electrical transport measurements show that the anomalous Hall angle increases with an increase of CoFeB layer thickness up to about 5 nm of CoFeB, after which it saturates with further increase of the thickness. This can be contrasted with the thickness dependence of the emitted THz amplitude, for which the increase up to about 5 nm is superseded by a decrease due to the Fabry–Perot cavity effect. Lastly, a detailed analysis of the results obtained from electrical transport measurements indicates that skew scattering is the dominant mechanism in our anomalous Hall effect-based CoFeB THz emitter.

## Methods

Thin films of CoFeB with different thicknesses ( $t_{\text{CoFeB}}$ ) were deposited at room temperature using a DC magnetron sputtering system equipped with a turbo pump achieving a base pressure of  $1 \times 10^{-10}$  Torr. The base pressure and working pressure of the chamber during deposition were  $5 \times 10^{-10}$  and  $2 \times 10^{-3}$  Torr, respectively where 99.999% pure Ar gas was used as a sputtering gas. Prior to the deposition, the single-side polished  $\text{Al}_2\text{O}_3$  substrates (thickness  $\sim 0.5$  mm) were preheated at base pressure to 600 °C for 1 h and then cooled down to room temperature before deposition. Substrates were rotated at 6 rpm speed for uniform growth. The deposition rate of CoFeB was calibrated using XRR measurements. To protect the CoFeB layer from oxidation and provide an additional interface for the backflow current, a 3 nm thick Al cap layer was deposited. The Al cap becomes completely oxidized at ambient conditions.

In GIXRD, the  $\text{Cu K}\alpha$  X-ray radiation was incident on the emitters with an incident angle of  $\omega = 1^\circ$ . The GIXRD scans were performed in continuous scan mode with the scattering angle,  $2\theta$ , in the range of  $10^\circ$ – $75^\circ$ .

A THz time-domain spectrometer was used to measure the THz emission from the CoFeB films<sup>15,30,31</sup>. A Spectra-Physics Tsunami (Ti: sapphire) was used as a laser source, which delivers pulses of  $\sim 55$  fs duration (bandwidth  $\sim 12$  nm, central wavelength  $\sim 800$  nm, and maximum output energy  $\sim 10$  nJ) at a repetition rate of 80 MHz. A low-temperature gallium arsenide photoconductive dipole antenna with  $\sim 4$   $\mu\text{m}$  gap was used as a detector for the THz pulses. A probe beam with average laser power of 10 mW was used for detection and a static in-plane magnetic field of  $\sim 85$  mT was used to saturate the magnetization of the CoFeB films. The displayed THz signals in Fig. 3a correspond to averages of 500 detected THz spectra obtained within one minute of measurement time.

The Quantum Design physical property measurement and magnetic properties measurement systems were employed to measure the AHE and the saturation magnetization of the CoFeB-based emitters, respectively. For AHE measurements, Hall bar devices ( $20 \times 100$   $\mu\text{m}^2$ ) were patterned using optical lithography.

## Data availability

The datasets used and/or analyzed during the current study are available from the corresponding author on reasonable request.

Received: 20 February 2023; Accepted: 7 April 2023

Published online: 12 April 2023

## References

- Valušis, G., LISAUSKAS, A., Yuan, H., Knap, W. & Roskos, H. G. Roadmap of terahertz imaging 2021. *Sensor* **21**, 4092. <https://doi.org/10.3390/s21124092> (2021).
- Federici, J. & Moeller, L. Review of terahertz and subterahertz wireless communications. *J. Appl. Phys.* **107**, 6. <https://doi.org/10.1063/1.3386413> (2010).
- Smith, P. R., Auston, D. H. & Nuss, M. C. Subpicosecond photoconducting dipole antennas. *IEEE J. Quantum Electron.* **24**, 255–260. <https://doi.org/10.1109/3.121> (1988).
- Venkatesh, M., Rao, K. S., Abhilash, T. S., Tewari, S. P. & Chaudhary, A. K. Optical characterization of GaAs photoconductive antennas for efficient generation and detection of terahertz radiation. *Opt. Mater.* **36**, 596–601. <https://doi.org/10.1016/j.optmat.2013.10.021> (2014).
- Lepeshov, S., Gorodetsky, A., Krasnok, A., Rafailov, E. & Belov, P. Enhancement of terahertz photoconductive antenna operation by optical nanoantennas. *Laser Photonics Rev.* **11**, 1600199. <https://doi.org/10.1002/lpor.201600199> (2017).
- Jazbinsek, M., Puc, U., Abina, A. & Zidansek, A. Organic crystals for THz photonics. *Appl. Sci.* **9**, 882. <https://doi.org/10.3390/app9050882> (2019).

7. VEDIYAPPAN, S. *et al.* Evaluation of linear and nonlinear optical properties of d- $\pi$ -a type 2-amino-5-nitropyridinium dihydrogen phosphate (2A5NPDP) single crystal grown by the modified sankaranarayanan-ramasamy (sr) method for terahertz generation. *Cryst. Growth Des.* **19**, 6873–6892. <https://doi.org/10.1021/acs.cgd.9b00382> (2019).
8. Yang, Z. *et al.* Large-size bulk and thin-film stilbazolium-salt single crystals for nonlinear optics and THz generation. *Adv. Funct. Mater.* **17**, 2018–2023. <https://doi.org/10.1002/adfm.200601117> (2007).
9. Kim, K.-Y., Glowina, J. H., Taylor, A. J. & Rodriguez, G. Terahertz emission from ultrafast ionizing air in symmetry-broken laser fields. *Opt. Express* **15**, 4577–4584. <https://doi.org/10.1364/OE.15.004577> (2007).
10. Yan, D. *et al.* High-average-power, high-repetition-rate tunable terahertz difference frequency generation with GaSe crystal pumped by 2  $\mu$ m dual-wavelength intracavity ktp optical parametric oscillator. *Photonics Res.* **5**, 82–87. <https://doi.org/10.1364/PRJ.5.000082> (2017).
11. Lu, C., Zhang, C., Zhang, L., Wang, X. & Zhang, S. Modulation of terahertz-spectrum generation from an air plasma by tunable three-color laser pulses. *Phys. Rev. A* **96**, 053402. <https://doi.org/10.1103/PhysRevA.96.053402> (2017).
12. Bagley, J. D., Moss, C. D., Sorenson, S. A. & Johnson, J. A. Laser-induced plasma generation of terahertz radiation using three incommensurate wavelengths. *J. Phys. B At. Mol. Opt. Phys.* **51**, 144004. <https://doi.org/10.1088/1361-6455/aac6ef> (2018).
13. Fülöp, J. A., Tzortzakos, S. & Kampfrath, T. Laser-driven strong-field terahertz sources. *Adv. Opt. Mater.* **8**, 1900681. <https://doi.org/10.1002/adom.201900681> (2020).
14. Seifert, T. *et al.* Efficient metallic spintronic emitters of ultrabroadband terahertz radiation. *Nat. Photonics* **10**, 483–488. <https://doi.org/10.1038/nphoton.2016.91> (2016).
15. Gupta, R. *et al.* Co<sub>2</sub>FeAl full heusler compound based spintronic terahertz emitter. *Adv. Opt. Mater.* **9**, 2001987. <https://doi.org/10.1002/adom.202001987> (2021).
16. Beaurepaire, E., Merle, J.-C., Daunois, A. & Bigot, J.-Y. Ultrafast spin dynamics in ferromagnetic nickel. *Phys. Rev. Lett.* **76**, 4250–4253. <https://doi.org/10.1103/PhysRevLett.76.4250> (1996).
17. Zhang, W. *et al.* Ultrafast terahertz magnetometry. *Nat. Commun.* **11**, 1–9. <https://doi.org/10.1038/s41467-020-17935-6> (2020).
18. Beaurepaire, E. *et al.* Coherent terahertz emission from ferromagnetic films excited by femtosecond laser pulses. *Appl. Phys. Lett.* **84**, 3465–3467. <https://doi.org/10.1063/1.1737467> (2004).
19. Kampfrath, T. *et al.* Terahertz spin current pulses controlled by magnetic heterostructures. *Nat. Nanotechnol.* **8**, 256–260. <https://doi.org/10.1038/nnano.2013.43> (2013).
20. Yang, Y. *et al.* Anomalous Hall magnetoresistance in a ferromagnet. *Nat. Commun.* **9**, 1–9. <https://doi.org/10.1038/s41467-018-04712-9> (2018).
21. Zhang, Q. *et al.* Terahertz emission from anomalous Hall effect in a single-layer ferromagnet. *Phys. Rev. Appl.* **12**, 054027. <https://doi.org/10.1103/PhysRevApplied.12.054027> (2019).
22. Liu, Y. *et al.* Separation of emission mechanisms in spintronic terahertz emitters. *Phys. Rev. B* **104**, 064419. <https://doi.org/10.1103/PhysRevB.104.064419> (2021).
23. Su, G. *et al.* Anomalous Hall effect in amorphous Co<sub>40</sub>Fe<sub>40</sub>B<sub>20</sub>. *Phys. Rev. B* **90**, 214410. <https://doi.org/10.1103/PhysRevB.90.214410> (2014).
24. Battiato, M., Carva, K. & Oppeneer, P. M. Superdiffusive spin transport as a mechanism of ultrafast demagnetization. *Phys. Rev. Lett.* **105**, 027203. <https://doi.org/10.1103/PhysRevLett.105.027203> (2010).
25. Battiato, M., Carva, K. & Oppeneer, P. M. Theory of laser-induced ultrafast superdiffusive spin transport in layered heterostructures. *Phys. Rev. B* **86**, 024404. <https://doi.org/10.1103/PhysRevB.86.024404> (2012).
26. Björck, M. & Andersson, G. Genx: An extensible X-ray reflectivity refinement program utilizing differential evolution. *J. Appl. Crystallogr.* **40**, 1174–1178. <https://doi.org/10.1107/S0021889807045086> (2007).
27. Torosyan, G., Keller, S., Scheuer, L., Beigang, R. & Papaioannou, E. T. Optimized spintronic terahertz emitters based on epitaxial grown Fe/Pt layer structures. *Sci. Rep.* **8**, 1311. <https://doi.org/10.1038/s41598-018-19432-9> (2018).
28. Nagaosa, N., Sinova, J., Onoda, S., MacDonald, A. H. & Ong, N. P. Anomalous Hall effect. *Rev. Mod. Phys.* **82**, 1539–1592. <https://doi.org/10.1103/RevModPhys.82.1539> (2010).
29. Seifert, T. S. *et al.* Frequency-independent terahertz anomalous Hall effect in DyCo<sub>5</sub>, Co<sub>32</sub>Fe<sub>68</sub>, and Gd<sub>27</sub>Fe<sub>73</sub> thin films from DC to 40 THz. *Adv. Mater.* **33**, 2007398. <https://doi.org/10.1002/adma.202007398> (2021).
30. Gupta, R. *et al.* Strain engineering of epitaxial Pt/Fe spintronic terahertz emitter. Preprint at <http://arxiv.org/abs/2110.01547> (2021).
31. Gupta, R. *Spin Current Generation in Magnetic Heterostructures and its Impact on Terahertz Emission: A Spin Dynamics Perspective*. Ph.D. thesis, Acta Universitatis Upsaliensis (2021).

## Acknowledgements

This work is supported by the Swedish Research Council (Grant Numbers 2021-04658, 2018-04918, and 2017-03725) and Olle Engkvists Stiftelse (Grant Number 182-0365).

## Author contributions

R.G. conceived the idea. P.R. deposited the film and perform the XRD and XRR measurements with the support from R.G. V.M. and R.G. performed terahertz measurements with input from A.R. R.B. fabricated the Hall bar devices. V.M. and R.G. performed anomalous Hall measurements. V.M. wrote the manuscript with support from R.G. All authors participated in the interpretation of data. P.S. and R.G. finalized the manuscript.

## Funding

Open access funding provided by Uppsala University.

## Competing interests

The authors declare no competing interests.

## Additional information

**Correspondence** and requests for materials should be addressed to P.S. or R.G.

**Reprints and permissions information** is available at [www.nature.com/reprints](http://www.nature.com/reprints).

**Publisher's note** Springer Nature remains neutral with regard to jurisdictional claims in published maps and institutional affiliations.



**Open Access** This article is licensed under a Creative Commons Attribution 4.0 International License, which permits use, sharing, adaptation, distribution and reproduction in any medium or format, as long as you give appropriate credit to the original author(s) and the source, provide a link to the Creative Commons licence, and indicate if changes were made. The images or other third party material in this article are included in the article's Creative Commons licence, unless indicated otherwise in a credit line to the material. If material is not included in the article's Creative Commons licence and your intended use is not permitted by statutory regulation or exceeds the permitted use, you will need to obtain permission directly from the copyright holder. To view a copy of this licence, visit <http://creativecommons.org/licenses/by/4.0/>.

© The Author(s) 2023